International Journal of Multiphase Flow 172 (2024) 104729

Contents lists available at ScienceDirect

International Journal of Multiphase Flow

journal homepage: www.elsevier.com/locate/ijmulflow

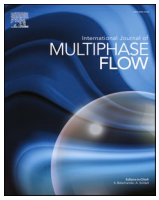

Equilibrium shape of a bubble in a liquid-filled horizontal capillary

Zefeng Jing [a,*], Chenchen Feng [b], John Ryan-Purcell [c], Stefan Hutzler [c]

[a] Key Laboratory of Thermo-Fluid Science and Engineering of MOE, School of Energy and Power Engineering, Xi'an Jiaotong University, Xi'an, Shaanxi, China
[b] School of Safety Science and Engineering, Xi'an University of Science and Technology, Xi'an, China
[c] School of Physics, Trinity College Dublin, The University of Dublin, Dublin, Ireland

ARTICLE INFO

Keywords:
Bubble in capillary
Carbon sequestration
Morse-Witten model
Surface Evolver

ABSTRACT

Bubbles in liquid-filled capillaries feature in many practical applications. Here we describe the equilibrium shape of a bubble in a horizontal capillary of circular cross section, as computed numerically using energy minimization. The data is presented in terms of empirical scaling laws for bubble extension along and perpendicular to the tube axis, over a large range of the ratio of cylinder to bubble diameter and Bond numbers. We also consider the limiting case of a bubble underneath a flat plate, for which approximate analytical solutions are available. Furthermore, we deduce an equation for the mean curvature of the gas–liquid interface and the variation of contact areas, the latter being of relevance also for estimating the wall drag forces of flowing bubbles.

1. Introduction

Static or quasi-static gas bubbles in liquid-filled capillaries feature prominently in many biological and engineering applications (Batchvarov et al., 2020; Esmaili et al., 2019; Khodaparast et al., 2017; Picchi et al., 2021), including oil-gas field development (Feng et al., 2022), soil remediation (Forel et al., 2019), and hydrogen production (Lake et al., 2022). A more recent application is bubble-assisted geological CO_2 sequestration (Føyen et al., 2020; Pandey et al., 2021), where gas bubbles are trapped in the capillary channels of a porous subsurface formation and thus increase the CO_2 storage capacity. The size and shape of these channels vary widely, affecting the bubble shape in these restricted spaces. Knowledge of the change in bubble pressure and film stresses in response to the local channel geometry (Jing and Feng, 2022; Jing et al., 2022), will help to understand the mobility of the CO_2 filled gas bubbles.

The case of an elongated bubble *moving* through a horizontal capillary has been widely investigated and is of relevance to microfluidics or lab-on-a-chip technology (Abbyad et al., 2011; Aquino et al., 2023; Arias and González-Cinca, 2016; Magnini et al., 2019, 2022; Murai et al., 2007; Perkins and Li, 2020). A circular cross-section of the capillary results in approximately cylindrical bubble shapes (Atasi et al., 2018; Zhao et al., 2018), with the formation of a thin liquid film separating the bubble from the capillary wall (Atasi et al., 2018). The variation in width h of this film as a function of bubble velocity has been widely studied and various empirical equations have been proposed (Chen et al., 2023), in particular for elongated bubbles (Atasi et al., 2017; Danov et al., 2021; Jones et al., 2021; Moran et al., 2021). Such work dates back to Taylor (Taylor, 1960), who showed that the ratio h/R_c (where R_c is the channel radius) asymptotes to 1/3 for $Ca \to 2$. Here Ca is the dimensionless capillary number, $Ca = \mu v_b/\sigma$, where μ is the viscosity of the liquid, v_b is the bubble velocity, and σ is the surface tension of the gas–liquid interface. Subsequently, more detailed descriptions of the shape of the bubble, and thus the local thickness of the liquid film surrounding it have been obtained, together with respective scaling relations (Atasi et al., 2018; Chen et al., 2023).

However, up to now, a detailed quantitative description of the equilibrium shape of a *static* bubble (Ca =0) in the curved confinement of a capillary has been missing. In the static case, forces exerted on a bubble in equilibrium in a liquid-filled capillary are due to buoyancy, surface tension and contact with the wall. Unlike hard spheres, bubbles are deformable and will adapt their shape to the given confinement. The balance between surface energy and gravitational energy (buoyancy) is expressed in terms of the dimensionless Bond number, $Bo = \Delta\rho g R_b^2/\sigma$, which determines the bubble shape (R_b is the radius of an undeformed spherical bubble, $\Delta\rho$ is the density difference between liquid and gas, and g is acceleration due to gravity). Hard spheres correspond to the limit $Bo \to 0$; the larger the Bond number, the more deformable or "softer" the bubbles are. The shape of a bubble thus depends on both the geometry of the confinement and the Bond number.

In particular bubbles of diameter smaller than the diameter of the capillary cannot be approximated by a cylinder. In this paper we will

* Corresponding author.
E-mail address: nyg201@foxmail.com (Z. Jing).

https://doi.org/10.1016/j.ijmultiphaseflow.2024.104729
Received 6 July 2023; Received in revised form 19 November 2023; Accepted 3 January 2024
Available online 5 January 2024

present descriptions of bubble shape in terms of bubble dimensions along and perpendicular to the axis of the capillary for a range of Bond numbers and size ratios, D_n, of cylinder to bubble diameter, $D_n = D_c/D_b$. The results are obtained via a minimization of the sum of surface and gravitational energies of the bubble. The limit $D_n \to \infty$, corresponding to a bubble underneath a flat plate, allows for analytical expressions describing its shape. These will be obtained from the Morse-Witten model (Höhler and Weaire, 2019; Morse and Witten, 1993) (in the limit $Bo \to 0$) and from a simple geometrical model (in the limit $Bo \to \infty$). Furthermore, all our simulations and analytical results correspond to the case of static bubbles placed in a horizontal liquid-filled cylinder, with an infinitesimally thin liquid film where the bubble contacts the cylinder wall. The contact angle is set to zero. This is the simplest case that one can consider; modifications could include allowing for a finite contact angle and a finite thickness of the wetting film. In a dynamic situation bubbles may also break-up due to shear (Yan et al., 2023).

2. Computational methods and characterization of bubble shapes

In static/quasi-static mechanical equilibrium, the shape of a bubble in this channel is determined by energy minimization (Cox et al., 2023), which is similar to many processes in nature (Glushkova et al., 2023). Therefore, the energy minimum method is especially suitable for this quasi-static bubble system. The energy which we wish to minimize for given values of bubble and cylinder diameter is given by

$$E_{\text{total}} = \sigma \int\int_S ds - \int\int\int_V (\rho_l - \rho_g) g z dv \tag{1}$$

where the integrals are over the surface area S of the bubble and its volume V, respectively. The coordinate system is indicated in Fig. 1(a). The x-axis coincides with the cylinder axis, and z is pointing upwards, against the direction of gravity. The density of liquid and gas are denoted by ρ_l and ρ_g, respectively. For the case of a gas bubble in an aqueous surfactant solution, as considered in the following, ρ_g is negligible.

We use the Surface Evolver software (Brakke, 1992) to first set up the topology of a bubble constrained in a horizontal capillary, the constraint of which is given by $y^2+z^2 \le D_c^2/4$; see Fig. 1(a). Acceleration due to gravity, g, liquid density ρ_l, and bubble volume V are set at the outset, and are kept constant throughout the simulations. The curved bubble surface is represented as a tessellation of small flat triangles. The minimization of energy (Eq.(1)) proceeds via iterative movement of the vertices of these triangles under the constraints of conserved bubble volume and channel boundary (Ginot et al., 2019). We then refine the tessellation of the bubble surface and simultaneously apply the conjugate gradient algorithm to minimize its energy. A system is considered converged when further refinements and/or iterations of the conjugate gradient method yield only small improvements in the total energy, in our case the threshold for convergence is approximately 10^{-14}. This corresponds to a computation time on a home computer (CPU: i7-9700) of approximately 4 min.

Fig. 1(a) shows an example of a bubble for Bond number $Bo = 0.510$, channel diameter $D_c = 3$ mm and bubble volume $V = 0.01$ cm^3. The bubble is pressed upwards (positive z-direction) against the cylinder by buoyancy, while at the same time experiencing expansion in the lateral direction of the cylinder (x-direction) due to volume conservation. There is also expansion in the y-direction, however this is limited by the cylinder radius. The cross-sections in Fig. 1(b) and (c) illustrate how the bubble shape changes in response to a decrease in channel diameter. This is quantifiable by computing the maximal bubble extensions b_x, b_y and b_z in x, y and z direction, respectively. Their variation with cylinder diameter is shown in Fig. 1(d) and will be discussed below.

We have also repeated the studies for a range of different bubble diameters D_b, and thus Bond numbers, Bo, to explore the effect of bubble softness. Fig. 2(a) –(c) shows the dimensionless bubble extensions b_x/D_b, b_y/D_b and b_z/D_b as a function of the ratio D_n of cylinder to bubble diameter, $D_n = D_c/D_b$, for different values of Bo.

For $D_n \lessapprox 1$ (*i.e.*, a lower D_n), the bottom of the bubble is in contact with the cylinder, and thus $b_z/D_b = b_y/D_b = D_n$, which can be seen from the insets in Fig. 2(b) and (c). Conservation of volume requires that b_x/D_b diverges ($\to \infty$) for $D_n \to 0$, as the bubble elongates in the direction of the cylinder axis. In this regime the bubble may be approximated as a sphero-cylinder (a cylinder with spherical caps at both ends, with the diameter of the cylinder (*i.e.* bubble) equal to that of the confining cylinder). In the limit $D_n \to \infty$ (the flat plate limit), symmetry dictates that b_x/D_b and b_y/D_b tend to the same asymptote (b_x/D_b is decreasing, b_y/D_b is increasing), whose value is determined by the Bond number Bo. Also the critical value D_n^*, at which the bottom of the bubble loses contact with the cylinder, depends on the Bond number; for hard spheres ($Bo = 0$), $D_n^*=1$, with smaller values for larger Bo. For values of D_n slightly larger than D_n^*, the vertical bubble extension b_z/D_b decreases with D_n, approaching a Bond number dependent asymptotic value which is less than that of the corresponding common asymptote for b_x/D_b and b_y/D_b. This decrease of b_z/D_b is driven by a lowering of the potential energy of the bubble. Additionally, in the context of liquid flow, $D_n > D_n^*$ marks the regime for which liquid can pass freely underneath the bubble, for smaller values the bubble blocks the cylinder.

The values of b_x/D_b, b_y/D_b and b_z/D_b in the *flat plate limit* ($D_n \to \infty$) depend on Bo, see Fig. 2(a)–(c). Fig. 2(d) shows the asymptotic values in the flat plate limit, $b_{x,\infty}$, $b_{y,\infty}$ and $b_{z,\infty}$, as a function of Bond number, Bo (the asymptotes $b_{x,\infty}$ and $b_{y,\infty}$ are identical, due to symmetry). This figure also shows results from a numerical solution of the Young-Laplace equation for a bubble underneath a flat plate, as obtained using a standard numerical algorithm (Pozrikidis, 2016). In the case of an axisymmetric bubble held under a plate by buoyancy, the Laplace-Young equation can be parametrized by defining the interface by a slope angle. The parametrised equation can then be solved using the shooting method to fulfil the constraint of volume conservation. The

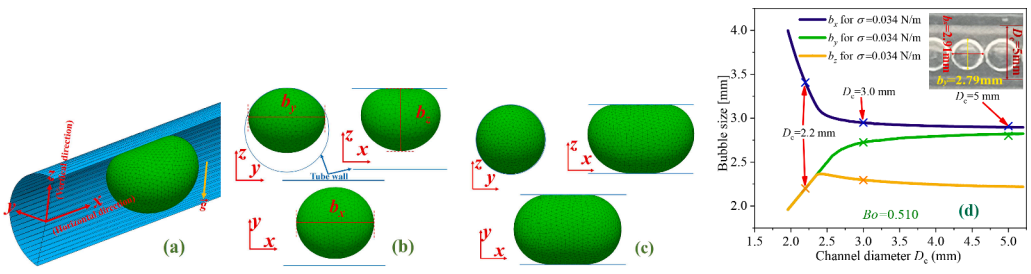

Fig. 1. (a) Surface Evolver simulation of a single bubble (Bo =0.510) resting in a liquid-filled horizontal cylinder. (b) and (c) Views from the x, y and z directions, respectively for simulations of a bubble of fixed volume 0.01 cm^3 (corresponding to $D_b = 2.67$ mm), placed in the cylinders of diameter $D_c = 3.0$ mm and $D_c = 2.2$ mm, respectively ($\sigma = 0.034$ N/m, $\rho_l = 1000$ kg/m^3, $g = 9.79$ m/s^2). (d) Variation of the maximal extensions in x,y and z direction, b_x, b_y, b_z, as a function of cylinder diameter, D_c. The inset shows a photograph of bubbles in a 0.2 wt% SDBS solution in a horizontal cylinder ($D_c = 5$ mm,$\sigma \approx 0.034$ N/m), used to provide some experimental data.

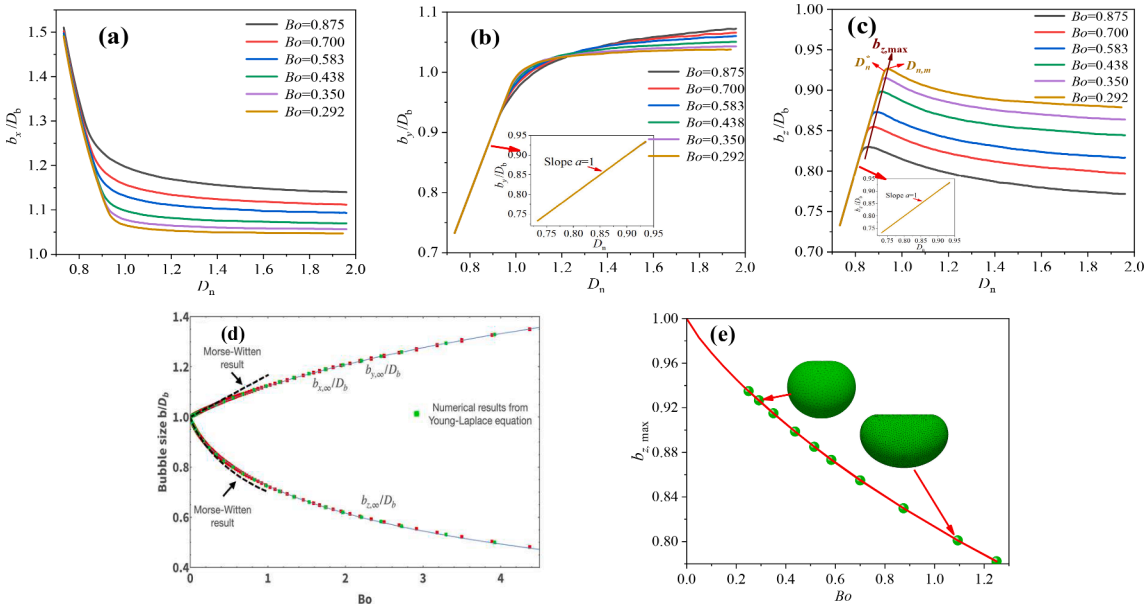

Fig. 2. (a)–(c) Dimensionless bubble extensions b_x/D_b, b_y/D_b and b_z/D_b as a function of $D_n = D_c/D_b$. D_n* denotes a critical value for D_n at which the continuous linear variation of the slope a =1 disappears, *i.e.*, the bottom of the bubble loses contact with the cylinder. For each of the *Bo* values, there is a corresponding D_n*. $D_{n,m}$ is the value of D_n at which b_z reaches a maximum $b_{z,\max}$. (d) Variation of the asymptotic values $b_{x,\infty}$, $b_{y,\infty}$ and $b_{z,\infty}$ with *Bo* in the limit $D_n \to \infty$, i.e., for a bubble underneath a flat plate as obtained from our simulations, numerical solutions of the Young-Laplace equation, and the Morse-Witten model. The solid lines are the semi-empirical relations of Eqs. (4) and (5). (e) Variation of the maximum of b_z, with *Bo*. The solid line shows the least square fit of Eq. (7). The flattening of the bubble for higher Bond number is clearly visible in the sample images that are shown.

computations are in excellent agreement with Surface Evolver calculations, see Fig. 2(d).

Analytical results for a bubble underneath a flat plate ($D_n \to \infty$) are available in the limits $Bo \to 0$ and $Bo \to \infty$. In the hard sphere limit, $Bo \to 0$, the model of Morse and Witten (Höhler and Weaire, 2019; Morse and Witten, 1993), which uses an approximation of the Laplace–Young equation in that limit, results in the following expressions for $b_x = b_y$ and b_z:

$$\frac{b_x}{D_b} = \frac{b_y}{D_b} = 1 + \frac{Bo}{6}; \qquad \frac{b_z}{D_b} = 1 + \frac{Bo}{6}\ln\left(\frac{Bo}{6}\right). \tag{2}$$

In the limit $Bo \to 0$, the expressions offer a good description of the data (see the dashed line in Fig. 2(d)). For Bo =0 the above expressions reduce to $b_{x,\infty}$= $b_{y,\infty}$= $b_{z,\infty}$= 1, corresponding to a spherical bubble shape.

In the limit $Bo \to \infty$, a bubble underneath a flat plate can be modelled as a surface of revolution of a stadium, *i.e.*, a rectangle with ends capped off with semicircles. Their radius of curvature is determined from the Laplace-Young equation. The pressure difference across the interface is set equal to the ratio of buoyancy force to the area of contact that this "pancake-type" bubble makes with the flat plate. Using volume conservation then results in the following two expressions, valid for $b_z/D_b << 1$, as in the case of large *Bo*.

$$\frac{b_x}{D_b} = \frac{b_y}{D_b} = \sqrt{\frac{2}{3}}Bo^{1/4}; \qquad \frac{b_z}{D_b} = \frac{1}{Bo^{1/2}}. \tag{3}$$

Combining the asymptotic expressions from both Morse-Witten and the pancake models yields the following empirical expression for b_x and b_y in the limit $D_n \to \infty$ as a function of *Bo*:

$$\frac{b_{x,\infty}}{D_b} = \frac{b_{y,\infty}}{D_b} = 1 + \frac{Bo}{6 + cBo^{\frac{3}{4}}}, \tag{4}$$

where the constant $c = \sqrt{3/2} \approx 1.22$, according to the limit form in Eq. (3). The solid line in Fig. 2(d) shows that the functional form of Eq. (4) provides an excellent description of our data. Here we determined the constant $c = 2.14$ from a least square fit of our data over the range $0 \leq Bo \leq 4.4$. In addition, the variation of $b_{z,\infty}$ over that same range of *Bo* can be described by the empirical form

$$\frac{b_{z,\infty}}{D_b} = \frac{1}{1 + 0.38Bo^{0.72}}. \tag{5}$$

We note that the fitted exponent of *Bo* exceeds the value of 1/2 as obtained from the pancake model for the limit $Bo \to \infty$ (Eq. (3)). This might be due to the fact that in this model the convex bottom of the bubble is approximated as being flat, which could affect the scaling of vertical bubble extension with *Bo*.

The vertical bubble extension b_z reaches a maximum at a value $D_{n,m}$, which is slightly higher than D_n*, see Fig. 2(c). $D_{n,m}$ can be described empirically as

$$D_{n,m} = \frac{1}{1 + 0.19Bo^{0.85}}. \tag{6}$$

The value of $b_{z,max} = b_z(D_{n,m})$ decreases with increasing *Bo,* as shown in Fig. 2(e), and is well described by the empirical expression

$$\frac{b_{z,\max}}{D_b} = \frac{1}{1 + 0.230Bo^{0.861}}. \tag{7}$$

The following heuristic expression, valid for $D_n \geq D_{n,m}$, is constructed, so as to fulfil the various limits $D_n = D_{n,m}(Bo)$, $D_n \to \infty$, $Bo \to 0$,

$$b_z - b_{z,\infty} = \frac{b_{z,\max} - b_{z,\infty}}{1 + c'(Bo)(D_n - D_{n,m})} \tag{8}$$

This describes all data shown in Fig. 2(c), with the pre-factor $c'(Bo)$ determined empirically as

$$c'(Bo) = \frac{4.0}{1 + 1.54Bo^{1.5}} \tag{9}$$

In Eq. (8), $b_{z,\infty}$, $b_{z,\max}$ and $D_{n,m}$ can be calculated by Eqs. (5), (7) and (6), respectively.

3. Mean curvature of the gas–liquid interface

Another approach to determining the shape of the bubble is to

examine the curvature along the interface. This is related to the gas pressure p in a bubble in a liquid by $p = p_{liq} + 2\sigma\kappa$, where κ is the mean curvature of the gas–liquid interface, with the pressure gradient in a static column of liquid given by $dp_{liq}/dz = -\rho g$. Generally, the pressure inside the bubble is treated as constant due to the negligible density of gas. Thus, for each point (x, y, z) on the bubble interface, $2\sigma\kappa - \rho g z = const.$ Here we are interested in the mean curvature κ_0 at the lowest position, z_0, of the bubble interface. For a given Bo and D_n, z_0 is readily obtained from Eq. (8): $z_0 = D_c/2 - b_z$, and we can thus determine the curvature at the lowest position of the bubble. Fig. 3(a) shows that κ_0 decreases monotonically for increasing D_n and Bo.

In Fig. 3(b) we show κ_0 as a function of Bo for a bubble underneath a flat plate. In the limit $Bo \to 0$, we can obtain an expression for the curvature from the Morse-Witten approach

$$\kappa_{0,\infty} D_b = \frac{2}{1 + \frac{5}{18} Bo}. \tag{10}$$

When $Bo = 0$, the bubble is a hard sphere and $\kappa_{0,\infty} = 1/R$. In this case, $\kappa_{0,\infty} D_b = 2$. In the limit $Bo \to \infty$, the curvature tends to zero. Fig. 3(b) shows a fit to

$$\kappa_{0,\infty} D_b = \frac{2}{1 + c_1 Bo + c_2 Bo^2}, \tag{11}$$

over the entire range of Bond numbers for which we carried out Surface Evolver simulations, resulting in $c_1 = 0.31$ and $c_2 = 0.05$. The prefactor c_1 is close to the value $5/18 \approx 0.28$, as predicted from the Morse-Witten expression for the limit $Bo \to 0$ (Eq. (10)). Numerical limitations of the Surface Evolver approach will also contribute to a deviation from the Morse-Witten result; the representation of the surface as a tessellation of triangular facets will unavoidably result in inaccuracies when computing a local curvature in the hard sphere limit ($Bo = 0$).

For values of $D_n \geq D_{n,m}$ the data in Fig. 3(a) is described by the following heuristic expression (of similar form to Eq.(8)),

$$\kappa_0 - \kappa_{0,\infty} = \frac{\kappa_{z,max} - \kappa_{0,\infty}}{1 + f(Bo)\left(D_n - D_{n,m}\right)} \tag{12}$$

with $\kappa_{z,max} = \frac{2}{1 + 0.223 Bo}$ and the pre-factor $f(Bo)$ determined empirically as $f(Bo) = \frac{10.96}{Bo}$.

Using $2\sigma\kappa - \rho g z = const$, the mean curvature at each point on the bubble interface which is not in contact with the channel can be expressed as

$$\kappa = \frac{\rho g (z - z_0)}{2\sigma} + \kappa_0. \tag{13}$$

This enables us to compute the mean curvature of each point on the gas–liquid interface of bubble, in good agreement with our simulation data in Fig. 3(c).

A potential method for determining the shape of the entire bubble interface analytically beyond the limits of the Morse-Witten model is to transform the mean curvature equation to spherical coordinates. Using the symmetry in the case of a bubble beneath a flat plate, we can set the lowest point of the bubble boundary as the coordinate origin and use spherical coordinates to describe the gas–liquid interface: $X(\theta, \varphi) = \phi(\theta)\sin\theta\cos\varphi$, $Y(\theta, \varphi) = \phi(\theta)\sin\theta\sin\varphi$ and $Z(\theta, \varphi) = \phi(\theta)\cos\theta$, where $\phi(\theta)$ is the distance between the origin and a point on the bubble boundary, θ is the angle between the line connecting the point to the origin and the vertical direction, and φ is the angle between the projection of this line on the X-0-Y plane and the X-axis. The mean curvature in this coordinate system is given by (Höhler and Weaire, 2019):

$$\kappa = \frac{\phi\phi'' - 3\phi'^2 - 2\phi^2}{2\left(\phi'^2 + \phi^2\right)^{3/2}} - \frac{\phi' \tan\theta}{2\phi\left(\phi'^2 + \phi^2\right)^{1/2}}. \tag{14}$$

Eqs. (13) and (14) could be combined to obtain exact equations for the interface of a bubble in a capillary channel, given appropriate boundary conditions.

4. Area of the gas–liquid interface

We have also computed the dimensionless excess area of a bubble, defined as $\varepsilon = S/S_0 - 1$, which is a measure of the deviation of the total surface area S of a bubble from that of an undeformed bubble, with $S_0 = 4\pi R_b^2$. In general, a "softer" bubble (higher values of Bo) results in larger deformation, as shown in Fig. 2(e), leading to an increase in surface area S. Plots of the excess surface area, ε, as a function of D_n for several Bond numbers are shown in Fig. 4(a). For fixed D_n, ε increases with Bo. The excess surface area is minimal for $D_n \approx 1$, increasing slightly in the limit $D_n \to \infty$. This asymptotic value increases with Bo, as shown in Fig. 4(b). Again, the limiting behavior (bubble underneath a flat plate) can be understood using the Morse–Witten model. In the hard sphere limit ($Bo \to 0$), the Morse–Witten model gives for the excess surface area of a bubble underneath a plate

$$\varepsilon(Bo) = \frac{Bo^2}{18}\left(\ln\left(\frac{6}{Bo}\right) - \frac{4}{3}\right), \tag{15}$$

which is in excellent agreement with the numerical data for $Bo \lesssim 0.5$, see Fig. 4(b). For Bond numbers $Bo > 0.5$, we find that the data is well described by the empirical form $\varepsilon(Bo) = 0.050Bo - 0.009$.

The total contact area, S_c, between the bubble and the channel, which depends on both cylinder diameter, D_n, and Bond numbers, was computed as follows. The Surface Evolver represents the bubble surface as a tessellation of triangular faces. In order for such a triangle to contribute to S_c, the x and y coordinates of each of its three edges (vertices) need to satisfy the constraint of the cylinder surface, i.e. $y^2 + z^2 = D_c^2/4$.

Fig. 5(a) shows that the value of S_c/S_0 decreases steadily with increasing D_n, as a larger cylinder diameter results in less deformation of the confined bubble (see also the inset of Fig. 3(c)). Softer bubbles (higher Bo) become more deformed when placed in a channel (or

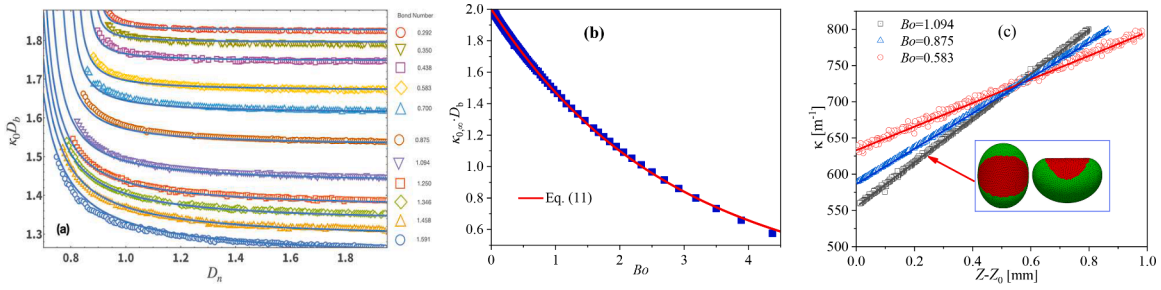

Fig. 3. (a) Dimensionless mean curvature at the lowest point of a bubble *vs* D_n for several values of Bond number Bo. The lines are given by Eq. (10). (b) Variation of the non-dimensionalised mean curvature with Bo in the flat plate limit, $D_n \to \infty$. The line results from a least-square fit to Eq. (11). (c) Variation of the mean curvature as a function of the vertical position along the liquid-gas interface ($D_b = 2.67$ mm, $D_c = 2.8$ mm). The lines are fits to Eq. (13) for different values of Bo. The part of the bubble marked in red denotes the contact with the channel wall.

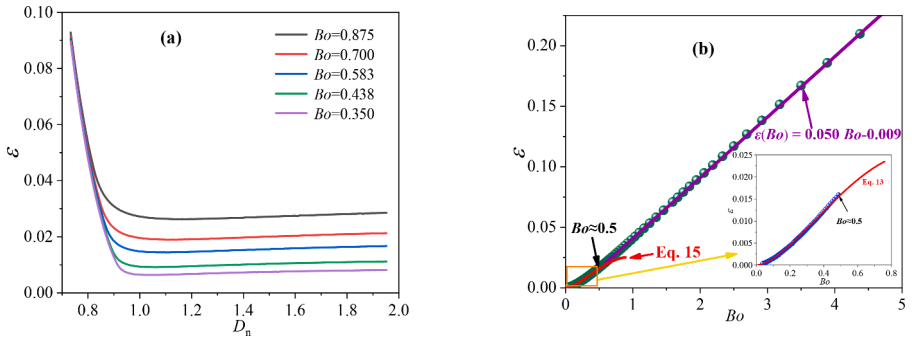

Fig. 4. (a) Variation of the dimensionless excess surface area ε of a bubble as a function of D_n for various Bond numbers. (b) Variation of ε with Bo for a bubble resting underneath a flat plate ($D_n \to \infty$). In the limit $Bo \to 0$ the excess energy is given by Eq. (15), as obtained from the Morse-Witten model (see also the inset). For higher Bond numbers, ε varies linearly over the range of Bond numbers investigated.

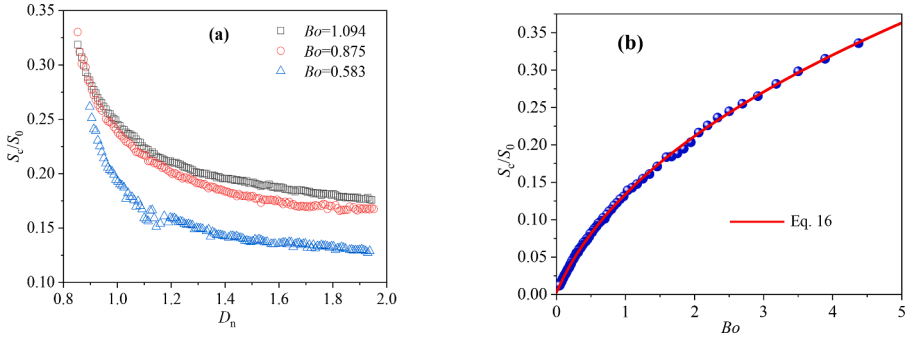

Fig. 5. (a) Variation of the contact area S_c/S_0 between the bubble and the channel as a function of D_n for three different values of Bond number. (b) In the flat plate limit ($D_n \to \infty$), S_c/S_0 is described by the empirical relation of Eq. (16), which is informed by the scaling in the limits of $Bo \to 0$ (Morse-Witten) and $Bo \to \infty$. A constant offset is included in this formula to account for the numerical limitation in the low Bo limit.

underneath a flat plate), than harder ones (lower Bo), leading to an increase of contact area with Bo.

In Fig. 5(b) we show the Bond number dependence of S_c (normalized by the surface area of a sphere, S_0) in the flat plate limit, $D_n \to \infty$. It is clear that our Surface Evolver data suffers from numerical limitations in the low Bond number limit, as the contact area S_c does not extrapolate to zero, as it must (contact of a hard sphere with a flat plate). As already observed above, this is a consequence of the triangulation of the surface.

Again we can take recourse to the Morse-Witten model in the low Bo limit to obtain the asymptotic form $S_c/S_0 = Bo/6$. This describes the data well in this limit, if we allow for an offset in S_c/S_0 of about 0.003 to account for numerical errors. In the limit $Bo \to \infty$, we obtain the scaling, $S_c/S_0 = \sqrt{Bo}/6$ from considering the contact area of the surface of revolution of a stadium as above. In Fig. 5(b) we show the empirical relation

$$\frac{S_c}{S_0} = \frac{Bo}{6(1 - 0.96Bo^{1/4} + 1.23Bo^{1/2})} + 0.003, \tag{16}$$

which has the correct scaling in both limits, and offers a good description of our numerical data.

5. Conclusions

We have presented simulations for the equilibrium shape of a (buoyant) gas bubble contained in a horizontal cylinder. The simulations, which were based on minimization of the sum of surface and gravitational energy, were carried out for a wide range of ratios of cylinder to bubble diameter, and Bond numbers up to $Bo \approx 4.5$. Analytical results were presented for the limiting case of a bubble held underneath a flat plate. Empirical expressions informed by limiting asymptotic behaviours are presented for quantities such as bubble-cylinder contact area, and the extension of bubble size along and perpendicular to the cylinder axis. The limit of $Bo \to 0$ was analyzed using analytical result of the Morse-Witten model. In this limit, the bubble shape deviates only slightly from that of a sphere, and the finite number of triangles in a Surface Evolver tessellation can affect the accuracy of the numerical results.

Our results should be of value for many practical applications. For example, the dependence of contact area as a function of Bond number and channel diameter will enter the computation of drag forces, at least in the limit of small bubble velocities. The case of a horizontal tube of uniform cylindrical cross-section is a first step towards the understanding of bubble shape in confinement. In many applications the bubbles are confined in a network of channels of arbitrary shape and orientation. However, the presented calculations and methods can be readily extended to the case of inclined tubes, and polygonal cross-sections.

The range of Bond numbers in our simulations, $Bo < 4.5$, is sufficient for many applications, including the storage of CO_2 in porous media mentioned in the introduction. For the much larger bubbles used in the experiments shown in Fig. 1(d), with bubble diameter $D_b = 2.7$ mm, we obtain $Bo \approx 0.510$, *i.e.*, a value that is well within the range of the present study.

CRediT authorship contribution statement

Zefeng Jing: Funding acquisition, Investigation, Methodology, Software, Writing – original draft. **Chenchen Feng:** Data curation, Formal analysis, Investigation, Writing – review & editing. **John Ryan-Purcell:** Formal analysis, Investigation, Writing – review & editing. **Stefan Hutzler:** Formal analysis, Funding acquisition, Investigation, Methodology, Writing – review & editing.

Declaration of competing interest

The authors declare that they have no known competing financial interests or personal relationships that could have appeared to influence the work reported in this paper.

Data availability

The data that has been used is confidential.

Acknowledgment

This work is supported by the Projects from the National Natural Science Foundation of China (No. 51706173), the Natural Science Basic Research Program of Shaanxi Province (Nos. 2023-JC-QN-0439 and 2023-JC-QN-0029), the China Postdoctoral Science Foundation (No. 2022M722556) and the Postdoctoral Science Foundation of Shaanxi Province (No. 2017BSHEDZZ43). SH and JR-P acknowledge support from the European Space Agency for the "Soft Matter Dynamics" projects, contracts 4000115113 and 4000129502. The authors thank Professor Ken Brakke for support with the Surface Evolver method.

References

Abbyad, P., Dangla, R., Alexandrou, A., Baroud, C., 2011. Rails and anchors: guiding and trapping droplet microreactors in two dimensions. Lab Chip 11, 831-821.
Aquino, A., Picchi, D., Poesio, P., 2023. Dynamics of a Taylor bubble through a shear-thinning fluid up to finite capillary numbers. J. Non-Newton. Fluid Mech. 314, 105003.
Arias, S., González-Cinca, R., 2016. Analysis of the characteristic lengths in the bubble and slug flow regimes generated in a capillary T-junction. Int. J. Multiph. Flow 87, 167–174.
Atasi, O., et al., 2018. How to measure the thickness of a lubrication film in a pancake bubble with a single snapshot? Appl. Phys. Lett. 113 (17), 173701.
Atasi, O., Khodaparast, S., Scheid, B., Stone, H.A., 2017. Effect of buoyancy on the motion of long bubbles in horizontal tubes. Phys. Rev. Fluids 2 (9), 094304.
Batchvarov, A., et al., 2020. Effect of surfactant on elongated bubbles in capillary tubes at high Reynolds number. Phys. Rev. Fluids 5 (9), 093605.
Brakke, K.A., 1992. The surface evolver. Exp. Math. 1 (2), 141–165.
Chen, C., et al., 2023. Two-phase flow and morphology of the gas–liquid interface for bubbles or droplets in different microchannels. Phys. Fluids 35 (9), 091302.
Cox, S.J., Davarpanah, A., Rossen, W.R., 2023. Interface shapes in microfluidic porous media: conditions allowing steady, simultaneous two-phase flow. Transp. Porous Media 147 (1), 197–216.
Danov, K.D., Lyutskanova-Zhekova, G.S., Smoukov, S.K., 2021. Motion of long bubbles in gravity- and pressure-driven flow through cylindrical capillaries up to moderate capillary numbers. Phys. Fluids 33 (11), 113606.
Esmaili, E., Shukla, P., Eifert, J.D., Jung, S., 2019. Bubble impact on a tilted wall: removing bacteria using bubbles. Phys. Rev. Fluids 4 (4), 043603.
Feng, C., Ma, X., Jing, Z., 2022. Dynamic proppant-carrying performance of VES-CO_2 foam fracturing fluid in the pipeline and the fracture. J. Petrol. Sci. Eng. 210, 110034.
Forel, E., Dollet, B., Langevin, D., Rio, E., 2019. Coalescence in two-dimensional foams: a purely statistical process dependent on film area. Phys. Rev. Lett. 122 (8), 088002.
Føyen, T., Brattekås, B., Fernø, M.A., Barrabino, A., Holt, T., 2020. Increased CO_2 storage capacity using CO_2-foam. Int. J. Greenh. Gas Control 96, 103016.
Ginot, G., Höhler, R., Mariot, S., Kraynik, A., Drenckhan, W., 2019. Juggling bubbles in square capillaries: an experimental proof of non-pairwise bubble interactions. Soft Matter 15 (22), 4570–4582.
Glushkova, D., et al., 2023. Drop shape stability vs shape shifting: role of surfactant adsorption layer. Colloids Surf. A: Physicochem. Eng. Asp. 656, 130374.
Höhler, R., Weaire, D., 2019. Can liquid foams and emulsions be modeled as packings of soft elastic particles? Adv. Colloid Interface Sci. 263, 19–37.
Jing, Z., Feng, C., 2022. Influence mechanisms of several parameters on the interaction between flowing wet foam and settling particle. Int. J. Multiph. Flow 150, 104015.
Jing, Z., Feng, C., Ma, X., Xu, D., Wang, S., 2022. Mechanical evolution of bubble structure and interactive migration behaviors of two particles in flowing wet foam. J. Rheol. 66 (2), 349–364.
Jones, T.J., Jambon-Puillet, E., Marthelot, J., Brun, P.T., 2021. Bubble casting soft robotics. Nature 599 (7884), 229–233.
Khodaparast, S., Kim, M.K., Silpe, J.E., Stone, H.A., 2017. Bubble-driven detachment of bacteria from confined microgeometries. Environ. Sci. Technol. 51 (3), 1340–1347.
Lake, J.R., Soto, Á.M., Varanasi, K.K., 2022. Impact of bubbles on electrochemically active surface area of microtextured gas-evolving electrodes. Langmuir 38 (10), 3276–3283.
Magnini, M., Khodaparast, S., Matar, O.K., Stone, H.A., Thome, J.R., 2019. Dynamics of long gas bubbles rising in a vertical tube in a cocurrent liquid flow. Phys. Rev. Fluids 4 (2), 023601.
Magnini, M., Municchi, F., El Mellas, I., Icardi, M., 2022. Liquid film distribution around long gas bubbles propagating in rectangular capillaries. Int. J. Multiph. Flow 148, 103939.
Moran, H.R., Magnini, M., Markides, C.N., Matar, O.K., 2021. Inertial and buoyancy effects on the flow of elongated bubbles in horizontal channels. Int. J. Multiph. Flow 135, 103468.
Morse, D.C., Witten, T.A., 1993. Droplet elasticity in weakly compressed emulsions. Europhys. Lett. 22 (7), 549.
Murai, Y., Fukuda, H., Oishi, Y., Kodama, Y., Yamamoto, F., 2007. Skin friction reduction by large air bubbles in a horizontal channel flow. Int. J. Multiph. Flow 33 (2), 147–163.
Pandey, A., Sinha, A.S.K., Chaturvedi, K.R., Sharma, T., 2021. Experimental investigation on effect of reservoir conditions on stability and rheology of carbon dioxide foams of nonionic surfactant and polymer: Implications of carbon geo-storage. Energy 235, 121445.
Perkins, S.J., Li, H.A., 2020. Elongated bubble centring in horizontal gas–liquid slug flow. Int. J. Multiph. Flow 123, 103158.
Picchi, D., Ullmann, A., Brauner, N., Poesio, P., 2021. Motion of a confined bubble in a shear-thinning liquid. J. Fluid Mech. 918, A7.
Pozrikidis, C., 2016. Fluid Dynamics: Theory, Computation, and Numerical Simulation. Springer.
Taylor, G.I., 1960. Deposition of a viscous fluid on a plane surface. J. Fluid Mech. 9 (2), 218–224.
Yan, S.l., Wang, X.q., Zhu, L.t., Zhang, X.b., Luo, Z.h., 2023. Mechanisms and modeling of bubble dynamic behaviors and mass transfer under gravity: a review. Chem. Eng. Sci. 277, 118854.
Zhao, B., Alizadeh Pahlavan, A., Cueto-Felgueroso, L., Juanes, R., 2018. Forced wetting transition and bubble pinch-off in a capillary tube. Phys. Rev. Lett. 120 (8), 084501.